PNAS RESEARCH ARTICLE | EARTH, ATMOSPHERIC, AND PLANETARY SCIENCES

Mineral carbonation of peridotite fueled by magmatic degassing and melt impregnation in an oceanic transform fault

Frieder Klein[a,1,2,3], Timothy Schroeder[b,1], Cédric M. John[c,3], Simon Davis[c], Susan E. Humphris[d], Jeffrey S. Seewald[a], Susanna Sichel[e], Wolfgang Bach[f], and Daniele Brunelli[d,g]

Edited by Peter Kelemen, Lamont-Doherty Earth Observatory, Palisades, NY; received September 8, 2023; accepted November 27, 2023

Most of the geologic CO_2 entering Earth's atmosphere and oceans is emitted along plate margins. While C-cycling at mid-ocean ridges and subduction zones has been studied for decades, little attention has been paid to degassing of magmatic CO_2 and mineral carbonation of mantle rocks in oceanic transform faults. We studied the formation of soapstone (magnesite–talc rock) and other magnesite-bearing assemblages during mineral carbonation of mantle peridotite in the St. Paul's transform fault, equatorial Atlantic. Clumped carbonate thermometry of soapstone yields a formation (or equilibration) temperature of 147 ± 13 °C which, based on thermodynamic constraints, suggests that $CO_{2(aq)}$ concentrations of the hydrothermal fluid were at least an order of magnitude higher than in seawater. The association of magnesite with apatite in veins, magnesite with a $\delta^{13}C$ of −3.40 ± 0.04‰, and the enrichment of CO_2 in hydrothermal fluids point to magmatic degassing and melt-impregnation as the main source of CO_2. Melt-rock interaction related to gas-rich alkali olivine basalt volcanism near the St. Paul's Rocks archipelago is manifested in systematic changes in peridotite compositions, notably a strong enrichment in incompatible elements with decreasing MgO/SiO_2. These findings reveal a previously undocumented aspect of the geologic carbon cycle in one of the largest oceanic transform faults: Fueled by magmatism in or below the root zone of the transform fault and subsequent degassing, the fault constitutes a conduit for CO_2-rich hydrothermal fluids, while carbonation of peridotite represents a vast sink for the emitted CO_2.

oceanic transform faults | carbon cycling | mineral carbonation | oceanic mantle | magmatic degassing

Significance

We report widespread mineral carbonation of mantle rocks in an oceanic transform fault fueled by degassing of magmatic CO_2. The findings describe a previously unknown component of the geological carbon cycle in transform faults that represent one of three principal plate boundaries on Earth. The confluence of exhumed mantle rocks and CO_2-rich alkaline basalt formed through limited extents of melting characteristic of the St. Paul's transform fault, one of the largest transform faults in the Atlantic, may be a pervasive feature at oceanic transform faults in general. Because transform faults have not been accounted for in previous global CO_2 flux estimates, the mass transfer of magmatic CO_2 to the altered oceanic mantle and seawater may be larger than previously thought.

Global anthropogenic CO_2 emissions are estimated to be on the order of 36 Gt per year (1), dwarfing estimates of average geological emissions (0.26 Gt/a) to the atmosphere and hydrosphere (2–5). Yet, over geological timescales, emissions of CO_2 sourced from Earth's mantle have been pivotal in regulating Earth's climate and habitability, as well as the C-concentration in surface reservoirs, including the oceans, atmosphere, and lithosphere. Fault zones along plate margins form a global network and are primary loci of tectonic movements, seismicity, and CO_2 discharge (5–7). Mantle-derived CO_2 from magmatic degassing and decarbonation associated with metamorphism are the main sources of geologic CO_2 released at Earth's surface (3, 4, 6, 8). Widespread discharge of CO_2-rich fluids has long been recognized on land along volcanic arcs, orogenic belts, and continental rifts (9–11) and, more recently, mid-ocean ridges (2, 8, 12, 13). Estimates of the global CO_2 flux suggest that the amount of CO_2 emitted from Earth's solid interior (i.e., outgassing) is broadly in balance with the amount of CO_2 recycled via subduction of altered oceanic plates (3, 4, 7, 14). The annual CO_2 emissions at mid-ocean ridges are estimated to be 13 to 30 Mt while intraplate volcanoes may emit 6 to 65 Mt (7). Even though the total length of oceanic transform faults (~48,000 km) (15) rivals that of the global mid-ocean ridge system, it remains unclear whether oceanic transform faults are sources or sinks for CO_2.

In contrast to intermediate- and fast-spreading mid-ocean ridges, where the oceanic crust is 6 km thick on average, the oceanic crust at transform faults is much thinner or completely lacking because magma supply tends to be low. As a result of the low magma supply and tectonic movements, much of the seafloor along slow-slipping oceanic transform faults is composed of mantle peridotite (16, 17). The exposure of peridotite to hydrothermal fluids causes the dissolution of olivine, orthopyroxene, and clinopyroxene and the precipitation of secondary minerals which has important consequences for mass transfer between the ocean and the oceanic basement (18–20). Previous research has focused on serpentinization (i.e., the formation of serpentine-dominated rocks) and high-temperature alteration of peridotite at slow- and ultraslow-spreading mid-ocean ridges and transform faults (17, 18, 21–24). Mineral carbonation of peridotite, which can cause the formation of soapstone (a rock chiefly composed of magnesite and talc) and silica-carbonate rock, has received considerable attention

Author contributions: F.K. and T.S. designed research; F.K., T.S., C.M.J., S.D., S.E.H., J.S.S., and S.S. performed research; F.K., T.S., C.M.J., S.D., and W.B. contributed new reagents/analytic tools; F.K., T.S., C.M.J., and S.D. analyzed data; and F.K., T.S., C.M.J., S.E.H., J.S.S., W.B., and D.B. wrote the paper.

The authors declare no competing interest.

This article is a PNAS Direct Submission.

[1]F.K. and T.S. contributed equally to this work.

[2]To whom correspondence may be addressed. Email: fklein@whoi.edu.

[3]Present address: Digital Environment Research Institute, Queen Mary University of London, London E1 1HH, United Kingdom.

This article contains supporting information online at https://www.pnas.org/lookup/suppl/doi:10.1073/pnas.2315662121/-/DCSupplemental.

Published February 12, 2024.

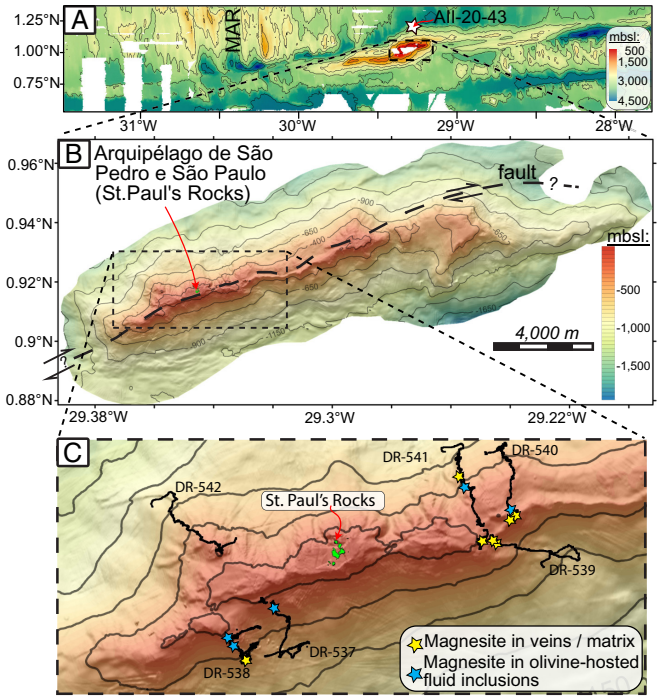

Fig. 1. (*A*) Map of the St. Paul's transform fault area compiled using bathymetric data collected during the COLMEIA cruise (34). MAR = Mid-Atlantic Ridge. Star indicates the location of dredge AII-20-43 containing vesicular alkali basalt. (*B*) Newly processed map acquired during cruise AL170602. Dashed line indicates location of transform fault. Dashed box indicates map area in panel *C*. (*C*) Detailed view of bathymetry, HOV dive tracks, and locations where magnesite-bearing rocks (yellow stars) and fluid inclusions (blue stars) were sampled with HOV *Deep Rover*.

in orogenic belts and ophiolites because of its enormous potential to sequester atmospheric CO_2 (25). Moreover, the formation of soapstone during carbonation of peridotite in continental transform faults is believed to promote aseismic creep, thereby limiting the potential for large earthquakes (26). Despite the widespread occurrence of peridotite in the Atlantic, Indian, and Arctic Oceans, and CO_2 emissions in the megaton range from mid-ocean ridges, few studies on magnesite formation during mineral carbonation of peridotite exist in submarine environments (27–30).

We document the formation of distinct carbon-bearing minerals including magnesite, dolomite, high-Mg calcite, calcite, aragonite, and graphite, their mineral assemblages, and textural contexts in peridotite from the submerged flanks of the St. Peter and St. Paul archipelago in the St. Paul's transform fault in the equatorial Atlantic Ocean (Fig. 1 and *SI Appendix*, Fig. S1). Based on isotopic and geochemical evidence, we argue that melt impregnation of peridotite and magmatic degassing of alkali olivine basalt is the source of CO_2 in the St. Paul's transform fault. We use clumped isotope paleothermometry of carbonate and graphite Raman thermometry to determine the temperatures of carbonation reactions and thermodynamic constraints to approximate the $CO_{2(aq)}$ concentrations of hydrothermal fluids that led to their formation. We argue that the combination of low extents of melting, which generates melts enriched in incompatible elements, volatiles and particularly CO_2 (31–33), and the presence of peridotites at oceanic transform faults creates conditions conducive to extensive mineral carbonation.

Results

Eighteen ultramafic rocks were collected using the human-occupied vehicles (HOV) *Deep Rover* and *Nadir* during Cruise AL170602 of MV *Alucia* in 2017. The rocks consist of harzburgite and clinopyroxene-poor lherzolite with varying extents of alteration and deformation. Ultramylonite samples show incipient alteration, whereas alteration tends to be more extensive in mylonite, protomylonite, and along brittle faults. The extent of alteration varies between samples that experienced similar extents of deformation, and within individual samples on a cm-scale. In addition to relict olivine, orthopyroxene, clinopyroxene, and Cr-spinel, which are characteristic of peridotite, several samples contain exotic minerals such as zircon, apatite, or rutile (*SI Appendix*, Table S1). Deformed pargasitic amphibole is rimmed by tremolite in the matrix of 16 of the 18 samples. Magnesite occurs in 12 of the studied samples: Six samples contain magnesite in the rock matrix, seven contain magnesite veins, and seven contain magnesite within secondary olivine-hosted fluid inclusions (*SI Appendix*, Fig. S3 and Table S1). Sample DR538-R1 is the most extensively carbonated sample examined in this study (Fig. 2 and *SI Appendix*, Fig. S1). Raman mapping of its matrix indicates that it is chiefly composed of talc and magnesite in roughly equal volumetric proportions, i.e., soapstone (Fig. 2 and *SI Appendix*, Fig. S1), with minor amounts of hematite and clay minerals. Sample DR538-R1 underwent pervasive carbonation that overprinted patches of talc-altered serpentinite. Here, magnesite and dolomite partially overprint serpentine, magnetite, and minor chlorite in mesh texture. Talc and magnesite mimic the rock's mylonitic foliation.

Carbonate veins are common in the studied ultramafic rocks, and feature one or more carbonate minerals including magnesite, dolomite, Mg-bearing calcite, calcite, and/or aragonite. Composite veins show spatially distinct mineralogical zones with Fe-bearing magnesite in the vein center, enveloped by dolomite, then high-Mg calcite, and finally calcite at the outermost part of the veins (Fig. 2). Some of the vein-hosted magnesite occurs together with chlorite and chrysotile (e.g., sample DR539-R2). Magnesite veins in sample DR539-R4 also contain traces of graphite. A large magnesite vein (sample DR539-R3) features small talc needles and talc veinlets (Fig. 2). Brittle (tension) faults are filled with aragonite (e.g., DR538-R2), which represent the youngest vein generation.

Samples DR539-R4 and DR541-R4 contain magnesite that is associated with apatite and chlorite (Fig. 2). We attempted to date apatite, but its U/Pb was too low (<10) to yield an age with a reasonable uncertainty. Sample DR541-R4 also contains biotite in veins with magnesite and apatite. Barite occurs in late carbonate veins that cut samples DR539-R3, DR541-R6, and DR542-R1.

Raman mapping revealed crystalline graphite together with talc and magnesite (e.g., sample DR538-R1) in the mylonite matrix together with olivine, orthopyroxene, and amphibole (e.g., DR538-R3, DR540-R1), and in veins together with magnesite, serpentine, and talc (e.g., DR540-R1). It is an accessory mineral in most samples; however, it can be locally abundant on a sub-millimeter scale.

Out of the 18 samples from St. Paul's Rocks (SPR) area studied here, nine contain olivine-hosted fluid inclusions that form linear trails equivalent to those reported in previous studies (19, 21, 35). Seven of the nine samples have fluid inclusions that either contain magnesite (n = 1) or assemblages composed of magnesite–talc (n = 2), magnesite–serpentine–talc (n = 2), magnesite–talc–graphite (n = 1), and magnesite–talc–graphite-CH_4 (n = 2) (*SI Appendix*, Fig. S3 and Table S1) on their inner walls. Fluid inclusions within an orthopyroxene porphyroclast of sample DR538-R3 contain talc and graphite. None of the secondary fluid inclusions in olivine or orthopyroxene contain liquid water (cf. refs. 19, 21, and 35). In samples DR539-R2, DR539-R3, and DR541-R2, magnesite and dolomite feature primary methane-bearing fluid inclusions.

Electron microprobe analysis was conducted on four samples to evaluate the composition of magnesite (*SI Appendix*, Table S2);

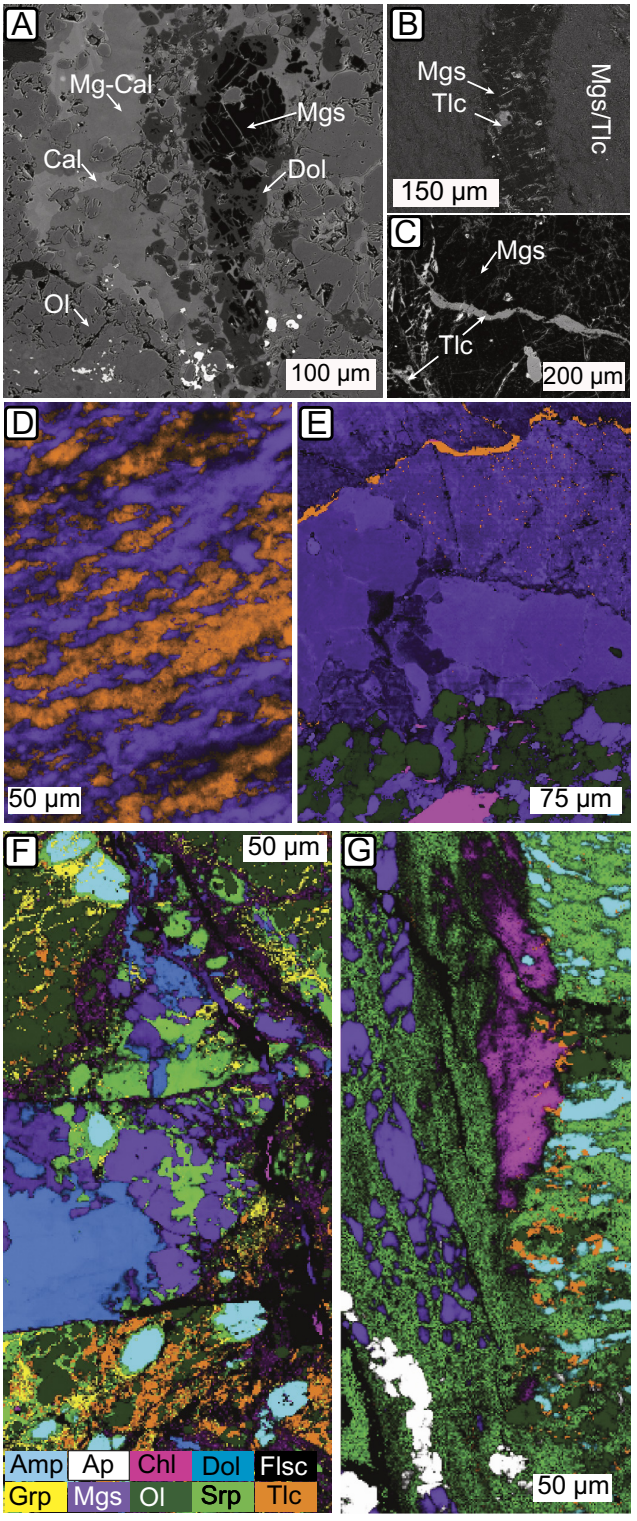

Fig. 2. Backscattered electron (BSE) images and hyperspectral Raman maps of magnesite mineralization in ultramafic rocks from the St. Paul's transform fault. BSE of composite carbonate vein (*A*) composed of magnesite (Mgs) in the vein center, rimmed by dolomite (Dol), Mg-calcite (Mg-Cal), and calcite (Cal) in mylonitized olivine (Ol). Zonation reflects changes in Mg/Ca of the hydrothermal fluid. Sample DR539-R3. (*B*) BSE image of vein composed of talc (Tlc) and magnesite (sample DR538-R1). (*C*) BSE images of talc vein cutting magnesite vein (DR539-R3). (*D*) Raman map of magnesite and talc in soapstone matrix (DR538-R1). Legend is the same as in (*F*) for all Raman maps. (*E*) Raman map of magnesite vein with minor talc adjacent to olivine and chlorite (Chl) (DR539-R3). (*F*) Raman map magnesite, talc, graphite (Grp), dolomite, amphibole (Amp), and olivine. Black indicates fluorescent (Flsc) background (DR540-R1). (*G*) Raman map of magnesite, chlorite, apatite (Ap), and minor talc associated with foliated olivine and amphibole (DR541-R4).

however, due to the (sub-)micrometer-scale intergrowth of magnesite and talc in the rock matrix, most microprobe analyses were done on magnesite in veins. The median Mg# (mol Mg/(Mg+Fe) × 100) of magnesite is 94, but there is considerable variability in the proportion of the siderite-component. Several analyses yielded Mg#s of ~80 to 85 while three analyses in DR538-R1 yielded Fe-enrichments with Mg#s of 61 and 74; however, there were no recognizable textural differences between Fe-poor and Fe-rich magnesite in these samples.

Whole rock major element measurements of peridotite mylonite samples are consistent with previous studies (36) and appear to follow the general melting array of submarine peridotites (*SI Appendix*, Fig. S2 and Tables S3 and S4); however, they tend to have higher Al_2O_3/SiO_2 ratios for a given MgO/SiO_2 ratio than (serpentinized) peridotites from other mid-ocean ridge settings (23, 24, 37, 38). Samples DR541-R4, DR541-R5, DR541-R6, and especially DR542-R5 (ophicalcite) are enriched in CaO due to calcite/aragonite veining. Rock compositions show enrichments in high-field-strength elements (HFSE) and large-ion lithophile elements (LILE) that are considered incompatible with mantle minerals (Fig. 3). Their enrichment is particularly apparent in rocks that have $MgO/SiO_2 < 1$. In contrast, concentrations of certain trace elements that are compatible in mantle minerals, such as Ni, decrease with decreasing MgO/SiO_2 (*SI Appendix*, Table S3).

Clumped isotopologue analysis of carbonate in sample DR538-R1 yields a $\Delta_{47\ CDES}$ value of 0.375 ± 0.011 ‰ (n = 3, mean ± 1σ SE), $\delta^{13}C$ = −3.40 ± 0.04‰, and $\delta^{18}O$ = −15.84 ± 0.34‰ relative to VPDB. The corresponding $\delta^{18}O$ of magnesite relative to VSMOW is 14.55 ± 0.29‰. Clumped carbonate thermometry suggests that the temperature at which magnesite formed or last equilibrated is 147 ± 13 °C (39) (*SI Appendix*, Table S5). Note that the matrix of sample DR538-R1 is dominated by magnesite (~50 vol.% based on hyperspectral Raman imaging) but also features small veins composed of dolomite, calcite, and/or aragonite.

Discussion

Conditions of Mineral Carbonation in Oceanic Peridotite. This study documents localized to pervasive magnesite formation arising from mineral carbonation of submarine-deformed peridotite in the vicinity of the SPR archipelago. Minerals that form during mineral carbonation provide a record of the environmental conditions that led to their formation, which can be deduced using thermodynamic tools. If (local) equilibrium is established and the temperature of mineral carbonation is known, thermodynamic phase relations can be used to approximate the composition of a fluid that co-exists with a magnesite-bearing mineral assemblage (29). Clumped isotope thermometry of soapstone yields a temperature of ~150 °C at which magnesite formed or last equilibrated. If magnesite was in local equilibrium with talc and assuming the activity "*a*" of H_2O = 1, $aCO_{2(aq)}$ in the hydrothermal fluid is bracketed by the invariant points of the mineral assemblages serpentine–talc–magnesite and quartz–talc–magnesite (29). At 150 °C and 50 MPa, which corresponds to a depth of ~1 to 1.5 km below the seafloor at a water depth of 1 km, thermodynamic phase relations suggest that $aCO_{2(aq)}$ must be higher than 0.002 (or ~2 mM assuming the activity coefficient of $CO_{2(aq)}$ is close to 1) and lower than 0.038 (or 38 mM) to stabilize magnesite and talc (29).

To provide additional constraints on the composition of the hydrothermal fluid that caused mineral carbonation of serpentinized

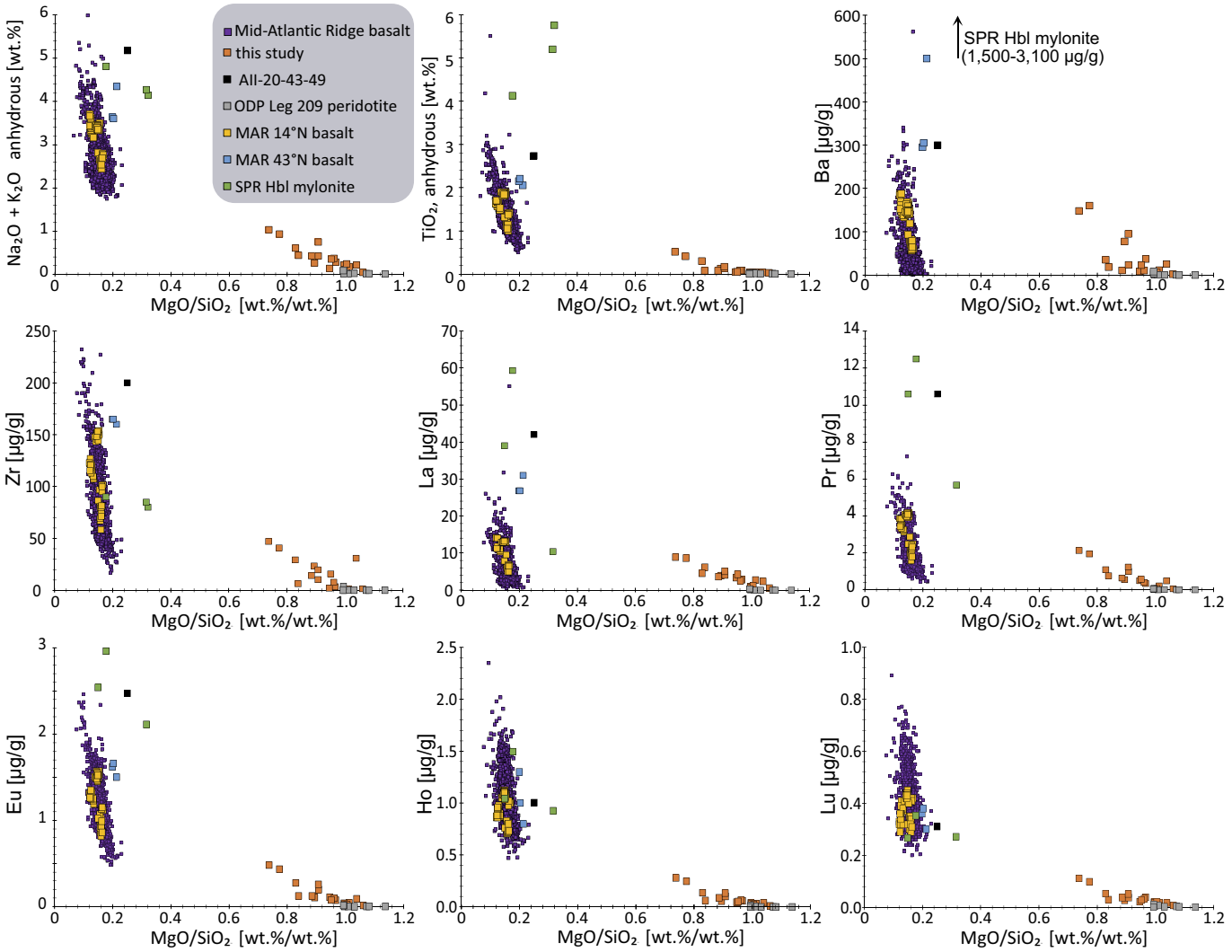

Fig. 3. Whole rock major and trace elements of peridotite mylonite from the SPR area in comparison to alkali olivine basalt (sample AII-20-43-49) and hornblende (Hbl) mylonite (both from the SPR area), highly vesicular basalt (popping rocks) from the 14°N and 43°N areas on the MAR, as well as normal MAR MORB. As the Mg/Si of SPR mylonite decreases the concentration of incompatible elements increase toward the composition of AII-20-43-49. See text for discussion.

peridotite, we calculated a thermodynamic reaction path model for carbonation of sample DR538-R1 (Fig. 4 and Dataset S1). To that end, we adopted a modeling approach where serpentinized harzburgite is allowed to react with a CO_2-enriched hydrothermal fluid at 150 °C and 50 MPa (29, 30). The predictions that most closely match our thin section observations (Fig. 2 and *SI Appendix*, Table S1), i.e., talc and magnesite in equal proportions with minor amounts of clay minerals and hematite, as well as a Mg# = 94 for magnesite (*SI Appendix*, Table S2), is at water/rock ratios of 246 to 277 where the predicted mineral assemblage is 43 to 47 vol. % talc and magnesite, each, 3.5 to 4 vol.% hematite, and 5 to 6.5 vol.% clay (saponite). Here, magnesite is predicted to host 638 to 667 kg CO_2 (22 to 23 wt.%) per m^3 of soapstone with a density of 2,900 kg/m^3. The predicted concentrations of $CO_{2(aq)}$ for this range are ~30 mM, i.e., on the higher end of the prediction that is based on the univariant phase equilibrium approach (29). The predicted in situ pH of 4.9 is slightly acidic compared to a neutral in situ pH of 5.7 at 150 °C and 50 MPa. The predicted Mg/Ca ratio of the fluid is initially low as serpentinization fluids tend to be depleted in Mg but enriched in Ca (40, 41) but the addition of a CO_2-enriched fluid releases Mg from brucite and serpentine, which causes an increase in the Mg/Ca ratio to ~5.3. When mineral carbonation ceases, the Mg/Ca of the fluid is expected to decrease, as recorded in zoned Mg–Ca carbonate veins of sample DR539-R3 (Fig. 2*A*). Serpentine and brucite buffer Si to low concentrations at moderate to low temperatures (42, 43). The addition of a CO_2-enriched fluid causes a strong increase in the concentration of dissolved Si due to the dissolution of silicate minerals and is effectively buffered by talc and magnesite at the modeled conditions (28, 30).

Because graphite occurs together with magnesite, serpentine, and talc in fluid inclusions of sample DR538-R3, graphite Raman thermometry can be applied to approximate the temperature of their formation (or peak exposure temperature) inside the inclusions. We used the program IFORS (Iterative Fitting of Raman Spectra) to deconvolute the D and G graphite Raman bands and generate curve functions that sum to the composite Raman spectrum (44) (*SI Appendix*, Tables S6 and S7). Temperatures calculated using empirical methods (45) for graphite in fluid inclusions of sample DR538-R3 range from 378 °C to 461 °C. If magnesite formed together with graphite, the minimum $CO_{2(aq)}$ concentration to form magnesite at the expense of olivine (defined by the invariant point olivine-brucite-magnesite if aH_2O is 1) at 378 °C and 50 MPa is ~150 mM. To stabilize magnesite together with talc at 375 °C and 50 MPa, the minimum CO_2 concentration is

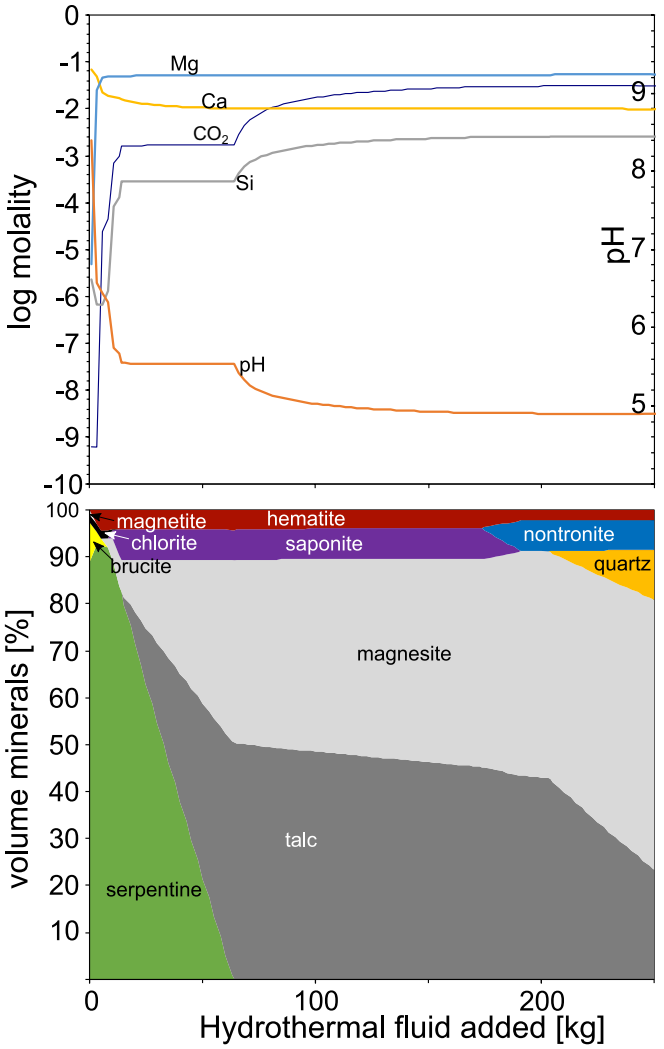

Fig. 4. Thermodynamic reaction path model for mineral carbonation of serpentinized peridotite. The model assumes that 1 kg of peridotite is serpentinized by 1 kg of heated seawater at 250 °C and 50 MPa (based on abundant magnetite in relict serpentinite in sample DR538-R1) and subsequently flushed with 250 kg of a CO_2-enriched hydrothermal fluid (52 mmol/kg) at 150 °C and 50 MPa (based on clumped carbonate thermometry). As the hydrothermal fluid is added to the serpentinite in small increments, both are allowed to equilibrate. This causes changes of the secondary mineralogy and the fluid composition. To reproduce the observed mineral assemblage and relative proportions of magnesite and talc, the model suggests that the concentration of $CO_{2(aq)}$ likely was about one order of magnitude higher than that of seawater (~30 mmol/kg) while the in situ pH was ~5. Notably, the concentration of dissolved Mg increases while that of Ca decreases as hydrothermal fluid is added, consistent with changes in Mg/Ca that influence the composition of carbonate minerals as, e.g., in Fig. 2*A*.

~1.6 M (29). If correct, CO_2 was at significantly higher concentration in the higher temperature hydrothermal fluid that was trapped in fluid inclusions than in the cooler fluid that caused pervasive magnesite formation in soapstone (~30 mM). However, graphite only forms in our model predictions if the formation of CH_4 is suppressed. Because CH_4 and graphite co-occur together with talc and magnesite inside olivine-hosted fluid inclusions (*SI Appendix*, Fig. S3), it seems likely that graphite can form when CH_4 formation is sluggish but not completely inhibited. Otherwise, our model predictions closely match the observed mineral assemblages, suggesting that the hydrothermal fluids responsible for mineral carbonation were strongly enriched in $CO_{2(aq)}$ over a wide range of temperatures from 150 °C to 375 °C. For comparison, hydrothermal fluids from the Main Endeavour Field on the intermediate-spreading Juan de Fuca ridge are strongly enriched in CO_2 (~100 mM) which has been attributed to degassing of basaltic magma (13, 46). While reported concentrations of $CO_{2(aq)}$ from hydrothermal systems at slow-spreading ridges are lower (e.g., 26 mM, 47), CO_2-saturated basalt (dubbed popping rocks) from the slow-spreading Mid-Atlantic Ridge (8, 48) attest that magmatic degassing is not limited to intermediate- or fast-spreading ridges and can conceivably lead to strong enrichments in hydrothermal vent fluids as well.

Melt Impregnation and Magmatic Degassing as the Likely Source of CO_2 for Mineral Carbonation. The principal sources of CO_2 in oceanic environments include seawater, metamorphic decarbonation of C-bearing sediments and altered oceanic crust, and magmatic degassing. The hydrothermal fluid in equilibrium with magnesite in sample DR538-R1 had a calculated $\delta^{18}O$ of 0.8 (*SI Appendix*, *Supporting Text*), similar to seawater-derived hydrothermal fluids emanating from submarine vents on the Mid-Atlantic Ridge (49, 50). However, the concentration of $CO_{2(aq)}$ in seawater is too low (~2.2 mmol/kg) to account for mineral carbonation of the studied samples. Metamorphic decarbonation of C-bearing sediments and altered oceanic crust, e.g., due to increasing pressure and temperature (as in subduction zones), seems unlikely to occur and cause widespread carbonation in oceanic transform faults. This leaves us with magmatic degassing as the probable source of CO_2 for mineral carbonation at an oceanic transform fault, an environment that, in general, is believed to be magma-poor relative to oceanic spreading centers.

An alkali olivine basalt lava flow from the northern flank of the SPR archipelago collected during cruise 20 of *RV Atlantis-II* (dredge 43) contains altered peridotite and peridotite mylonite xenoliths similar to the ones exposed at the SPR archipelago (36, 51–53). Its Quaternary age is indicative of recent (54), possibly ongoing magmatism in the area. The location of the eruption is ~130 km east of the spreading axis in crust that is approximately 7.8 to 8 Ma, suggesting that melt is (or recently was) present below the transform fault. At this distance, the low extent of melting in the "wings" of the melting region results in strong CO_2 and H_2O enrichments, as with other incompatible elements. Mantle flow away from the ridge axis and the long distance to the axis prevents focusing of these melts toward the ridge, leaving them stranded in the wings of the melting region (55). The melts can pool at the oceanic lithosphere–asthenosphere boundary in lenticular melt bodies (56) and subsequently impregnate the lithosphere (57) or they are extracted by small-scale convection (58), thereby contributing to off-axis magmatism (59).

Alkali olivine basalt in dredge 43 is highly vesicular suggesting that it was volatile-rich when emplaced. The CO_2 content of basalt before degassing can be reconstructed using the empirical relationship $CO_2/Ba = 81.3$ (5, 8). For the Ba concentration of sample AII-20-43-49 of ~300 µg/g (36), the calculated CO_2 content of undegassed basaltic melt would be 2.4 wt.%, even exceeding CO_2 concentrations of popping rocks from the 14°N area on the Mid-Atlantic Ridge (8, 12). Although we cannot rule out C-contributions from the peridotite precursor (i.e., before melt impregnation and mineral carbonation), the $\delta^{13}C$ value of magnesite −3.40 ± 0.04‰ likely reflects the $\delta^{13}C$ of the magmatic CO_2 enriched in the hydrothermal fluid from which magnesite precipitated. Notably, the measured value is virtually identical to that of one of the CO_2-richest popping rocks from the 14°N area (sample CR3-1, $\delta^{13}C$ = −3.44‰), similar to highly vesicular alkali basalt from the 34°50′N area on the MAR (48, 60) and consistent with mantle CO_2 as sampled by mid-ocean ridge basalt (MORB) glasses (61). In addition to these isotopic similarities, there is

geochemical and textural evidence for impregnation of peridotite by a basaltic melt prior to mylonitization. The ultramafic rocks examined in this study range in composition from depleted harzburgite to HFSE-, LILE-, and alkali-enriched harzburgite and lherzolite. Concentrations of Hf, Zr, Ti, Nb, and Ta as well as the REE increase with decreasing MgO/SiO_2 (Fig. 3). The compositions of alkali olivine basalt AII-20-43-49 from the northern submarine flank of the SPR archipelago, alkali olivine basalt from the 43°N transform valley (62), popping rocks from the 14°N area on the MAR (8), as well as MORB compositions compiled using the PetDB (EarthChem) database are shown for comparison. The increase in incompatible element concentrations toward the compositions of mafic rocks with decreasing MgO/SiO_2 suggests impregnation of peridotite by a melt with composition similar to the CO_2-rich alkali olivine basalt AII-20-43-49, which is consistent with REE patterns of clinopyroxene in peridotite (57). The crystallization of minerals, even hydrous minerals such as amphibole, during melt impregnation can cause enrichments of incompatible elements and CO_2 in percolating fluids. Melt impregnation and degassing may operate simultaneously or successively, depending on the depth at which melt impregnation occurs (or occurred); however, both processes can contribute CO_2 to drive mineral carbonation. The presence of deformed pargasitic amphibole porphyroclasts suggests melt-impregnation took place prior to mylonitization above the brittle-ductile transition temperature at ~700 °C (63). In this scenario, the enrichment of alkalis and REE as well as the formation of amphibole result from impregnation of peridotite by alkaline melts (57), and in contrast to previous suggestions (36, 52, 64, 65), the impregnated peridotite does not represent the source of the alkali basalt in the SPR area.

Where exactly melt impregnation took place cannot be answered unequivocally based on available age constraints. Considering the alkali basalt lava flow is of Quaternary age, it seems likely that melt impregnation took place recently. This is consistent with the low U/Pb ratios of apatite in sample DR541-R4. Moreover, melt-impregnation of peridotite is evident north and south of the transform fault trace which runs roughly E-W through the SPR massif. Because compositional trends suggest that one alkali-olivine basalt magma was responsible for melt impregnation, it seems unlikely that this would have happened at two conjugate Mid-Atlantic Ridge segments, North and South of the fault. Hence, we infer that melt impregnation took place close to the present location of SPR. Because pargasitic amphibole porphyroclasts underwent deformation during mylonitization, melt impregnation must have occurred above the brittle–ductile transition temperature, i.e., higher than 700 or 800 °C (66). Previous melting experiments on amphibole mylonite from SPR suggest that amphibole can be stable at the liquidus between 1 and 1.6 GPa with 2 wt.% water at 1,175 °C or with excess water between 1 and 2.1 GPa at 1,075 °C (67). While these constraints are consistent with melting in thick and cold lithosphere of the equatorial Atlantic (57, 68, 69), the exact pressure-temperature conditions of melt impregnation remain unknown.

Melt impregnation and the formation of amphibole prior to mylonitization is followed by fluid entrapment within olivine-hosted fluid inclusions, between ~400 and 600 °C (19). Raman thermometry of graphite in the mylonite matrix is consistent with fluid–rock interactions above 400°C (*SI Appendix*, Table S7) but at these temperatures thermodynamic phase relations suggest that extremely high $CO_{2(aq)}$ concentrations (>3.2 M) would be required for talc and magnesite to be stable (29), effectively preventing pervasive mineral carbonation of peridotite. As temperatures decrease, thermodynamic and kinetic constraints become favorable for mineral carbonation (29).

Prevalent Mineral Carbonation of Peridotite at Oceanic Transform Faults. The formation of carbonate minerals in oceanic mantle rocks typically involves calcite, aragonite, or dolomite. Magnesite is a major reaction product of ultramafic mineral carbonation in orogenic and in subduction-zone related continental settings but has rarely been reported from mid-ocean ridges (27). Magnesite can form during mineral carbonation in environments where peridotite or serpentinite interact with CO_2-enriched hydrothermal fluids. It is possible that the apparent lack of magnesite in most oceanic peridotite studied to date reflects a sampling bias or that the concentration of $CO_{2(aq)}$ from magmatic degassing is insufficient to create conditions conducive to widespread mineral carbonation.

While the undegassed CO_2 content of a normal MORB magma at oceanic spreading centers is significantly lower than that of alkali basalt (33), magmatically robust spreading centers are also devoid of peridotite exposures on the seafloor. Conversely, mantle-derived peridotites are abundant along transform faults and fracture zones because of the reduced magma production at the cold tip of oceanic spreading segments. Hence, it is plausible that magnesite formation during mineral carbonation could be prevalent in oceanic transform faults because of the confluence of CO_2-rich hydrothermal fluids from degassing of alkaline melts and the widespread presence of peridotite. Although the overall extent of mineral carbonation and the stored amount of CO_2 in ultramafic rocks at oceanic transform faults remains unknown, the potential for geological carbon sequestration in peridotite seems substantial considering that it can host several hundred kg of CO_2 per m^3 and that the overall length of oceanic transform faults rivals that of the global mid-ocean ridge system.

Our findings describe a previously unrecognized part of the geologic carbon cycle in oceanic transform faults. Limited extents of melting, magmatic degassing, and the resulting enrichments of CO_2 in percolating hydrothermal fluids cause mineral carbonation of mantle peridotite. While these processes have only been recognized at the St. Paul's transform fault thus far, they may be a pervasive feature at oceanic transform faults that connect slow- and ultraslow-spreading ridges because mantle peridotite is the dominant lithology and extents of melting are generally low. Hence, the mass transfer of magmatic CO_2 to the altered oceanic mantle and seawater may be larger than previously thought.

Materials and Methods

Peridotite mylonite samples from the submarine flanks of the SPR archipelago (also referred to as Arquipélago de São Pedro e São Paulo), St. Paul's transform fault, equatorial Mid-Atlantic Ridge, were collected using the HOV *Deep Rover* during cruise AL170602 of *MV Alucia*. The dive tracks and locations of the collected samples are indicated in Fig. 1. A bathymetric survey of the seafloor surrounding the archipelago was conducted using a Reson 7160 Multibeam system. Raw multibeam data were processed using MB-System software (70). Processed soundings were gridded with Surfer® (Golden Software, Golden, CO) using a nearest-neighbor algorithm to create a bathymetric map (Fig. 1, cf. ref. 71).

Thin sections were inspected in transmitted and reflected light using a petrographic microscope, with a scanning electron microscope (Hitachi TM3000) in backscattered electron (BSE) mode and using a confocal Raman microscope to determine their mineralogy in a microstructural context. Raman spectroscopy including hyperspectral Raman imaging was conducted using a Horiba LabRam HR system and a green (532 nm) laser, a grating with 600 grooves per mm, and a 100× objective with a numerical aperture of 0.9. The instrument was calibrated using the 520.7 cm^{-1} band of Si before and after each session. The acquired spectra were processed with the LabSpec 6 software suite and compared with reference spectra (72, 73) for identification of minerals.

A Cameca SX-100 electron microprobe analyzer at the University of Bremen (Germany) was used to determine the compositions of carbonate minerals. Samples were analyzed with a 15 keV accelerating voltage, 8 nA beam current, and a 10 μm spot size. Analytical conditions were checked for drift by analyzing calcite, dolomite, and siderite standards between every ~20 sample analyses.

Major and trace element analyses were performed using X-ray fluorescence and inductively coupled plasma mass spectrometry at the Peter Hooper GeoAnalytical Laboratory (University of Washington, Pullman, WA) using established methods (74–77).

The clumped isotope analysis and thermometry were performed at Imperial College, London, using the fully automated Imperial Batch EXtraction system following the method described by Adlan and John (78) and Adlan et al. (79). The standard-to-samples ratio used in our study is one standard for every three sample measurements. Mass 48 and mass 49 signal spikes were monitored for each measurement to detect hydrocarbons, chlorocarbons (80, 81), and sulfur-bearing contaminants (81, 82). To be deemed clean, a replicate analysis needed a Δ_{48} offset value <1.5‰ and/or a 49 parameter value <0.3 (83). Calculations and corrections of raw Δ_{47}, $\delta^{18}O$, and $\delta^{13}C$ were performed using the free software Easotope (84). Non-linearity in the mass spectrometer was corrected with the pressure baseline correction methods developed at ETH Zürich (85), and the Δ_{47} values projected in the inter-laboratory absolute reference frame or Intercarb Carbon Dioxide Equilibrated Scale (I-CDES) (86) based on our routinely measured ETH1, ETH2, ETH3, ETH4, and our internal Carrara marble carbonate standards (86–88). This Δ_{47} (I-CDES) was used to calculate the temperature of crystallization for the magnesite by applying a recent multi-lab calibration (89).

Reaction path models were calculated using the software package EQ3/6 (90) and a customized thermodynamic database for 50 MPa and 2 to 400 °C (22, 91). A pressure of 50 MPa would correspond to 1 to 2 km below the seafloor, depending on water depth and rock density (i.e., extent of alteration). The modeling approach was adapted from that used in Klein and Garrido (29). In brief, the in-situ equilibrium speciation of seawater was calculated for 250 °C, 50 MPa, and subsequently, 1 kg of the speciated fluid was allowed to equilibrate with 0.5 kg of peridotite (olivine : orthopyroxene : clinopyroxene = 80:15:5 vol.%) to form serpentinite. A temperature of 250 °C was chosen to account for the abundance of magnetite in relict serpentinite which formed prior to carbonation of sample DR538-R1. In the next step, seawater was heated to 150 °C and reacted with $CO_{2(aq)}$ to yield a hydrothermal fluid with a $CO_{2(aq)}$ concentration of 50 mM. In the last modeling step, 250 kg of the CO_2-enriched hydrothermal fluid was added in small increments to serpentinite to mimic mineral carbonation. Because the serpentinite was in equilibrium with 1 kg of the CO_2-poor fluid from the previous modeling step, and because some of the $CO_{2(aq)}$ reacted with serpentinite to form magnesite, the actual concentration at the end of the model run was 30.8 mM.

Data, Materials, and Software Availability. Dataset S1 data have been deposited in Zenodo (92). All other data are included in the manuscript and/or supporting information.

ACKNOWLEDGMENTS. The financial support for this study and shiptime aboard the *MV Alucia* was kindly provided by the Dalio Foundation through the Dalio Ocean Initiative (to F.K., S.E.H., and J.S.S.). Additional support for this project was provided by the Independent Research & Development Program at Woods Hole Oceanographic Institution (to F.K.) and by the NSF through EPSCoR RII Track-2 award #2033364 (to T.S.). We thank Cécile Prigent and an anonymous reviewer for their constructive comments, and Peter Kelemen for editorial handling. We thank Marcia Maia for kindly providing bathymetry data collected during the COLMEIA cruise. We would like to express our sincere gratitude to Captain Inglis, submersible team lead Alan Scott, the crew of the *MV Alucia*, and pilots of HOVs *Deep Rover* and *Nadir* for their outstanding work. Andrew Kylander-Clark is acknowledged for his help with dating apatite in sample DR541-R4.

Author affiliations: [a]Department of Marine Chemistry and Geochemistry, Woods Hole Oceanographic Institution, Woods Hole, MA 02543; [b]Natural Sciences Division, Bennington College, Bennington, VT 02543; [c]Department of Earth Science and Engineering, Imperial College London, London 02543, United Kingdom; [d]Department of Geology and Geophysics, Woods Hole Oceanographic Institution, Woods Hole MA 02543; [e]Laboratório de Geologia Marinha, Universidade Federal Fluminense, Niteroi 24210-340, Brazil; [f]Fachbereich Geowissenschaften and MARUM, Universität Bremen, Bremen 28359, Germany; and [g]Dipartimento di Scienze Chimiche e Geologiche, Università di Modena e Reggio Emilia, Modena 41125, Italy

1. P. Friedlingstein *et al.*, Global carbon budget 2021. *Earth Syst. Sci. Data* **14**, 1917–2005 (2022).
2. B. Marty, I. N. Tolstikhin, CO_2 fluxes from mid-ocean ridges, arcs and plumes. *Chem. Geol.* **145**, 233–248 (1998).
3. P. B. Kelemen, C. E. Manning, Reevaluating carbon fluxes in subduction zones, what goes down, mostly comes up. *Proc. Natl. Acad. Sci. U.S.A.* **112**, E3997 (2015).
4. T. Plank, C. E. Manning, Subducting carbon. *Nature* **574**, 343–352 (2019).
5. M. Le Voyer *et al.*, Carbon fluxes and primary magma CO_2 contents along the global mid-ocean ridge system. *Geochem. Geophys. Geosyst.* **20**, 1387–1424 (2019).
6. I. Barnes, W. P. Irwin, D. E. White, Global distribution of carbon dioxide discharges, and major fault zones of seismicity (U.S. Geological Survey Water-Resources Investigations, 1978), pp. 39–78.
7. K. Wong *et al.*, Deep carbon cycling over the past 200 million years: A review of fluxes in different tectonic settings. *Front. Earth Sci.* **7**, 263 (2019).
8. M. R. Jones *et al.*, New constraints on mantle carbon from Mid-Atlantic Ridge popping rocks. *Earth Planet. Sci. Lett.* **511**, 67–75 (2019).
9. I. Barnes, W. P. Irwin, H. A. Gibson, "Geologic map showing springs rich in carbon dioxide or chloride in California" (United States Geological Survey, Moffett Field, CA, 1975). https://www.usgs.gov/maps/geologic-map-showing-springs-rich-carbon-dioxide-or-or-chloride-california. Accessed 7 September 2016.
10. S. Brune, S. E. Williams, R. D. Müller, Potential links between continental rifting, CO_2 degassing and climate change through time. *Nat. Geosci.* **10**, 941–946 (2017).
11. T. P. Fischer *et al.*, The emissions of CO_2 and other volatiles from the world's subaerial volcanoes. *Sci. Rep.* **9**, 18716 (2019).
12. F. Pineau, M. Javoy, Strong degassing at ridge crests–The behaviour of dissolved carbon and water in basalt glasses at 14°N, Mid-Atlantic Ridge. *Earth Planet. Sci. Lett.* **123**, 179–198 (1994).
13. J. S. Seewald, A. Cruse, P. J. Saccocia, Aqueous volatiles in hydrothermal fluids from the Main Endeavour Field, northern Juan de Fuca ridge: Temporal variability following earthquake activity. *Earth Planet. Sci. Lett.* **216**, 575–590 (2003).
14. T. P. Fischer, A. Aiuppa, AGU centennial grand challenge: Volcanoes and deep carbon global CO_2 emissions from Subaerial Volcanism–Recent progress and future challenges. *Geochem. Geophys. Geosyst.* **21**, e2019GC008690 (2020).
15. P. Bird, An updated digital model of plate boundaries. *Geochem. Geophys. Geosyst.* **4**, 1027 (2003).
16. E. Bonatti, P. J. Michael, Mantle peridotites from continental rifts to ocean basins to subduction zones. *Earth Planet. Sci. Lett.* **91**, 297–311 (1989).
17. C. Prigent, J. M. Warren, A. H. Kohli, C. Teyssier, Fracture-mediated deep seawater flow and mantle hydration on oceanic transform faults. *Earth Planet. Sci. Lett.* **532**, 115988 (2020).
18. M. Cannat, F. Fontaine, J. Escartin, "Serpentinization and associated hydrogen and methane fluxes at slow spreading ridges" in *Diverstiy of Hydrothermal Systems on Slow Spreading Ocean Ridges*, P. A. Rona, C. W. Devey, J. Dyment, B. J. Murton, Eds. (*Geophysical Monograph Series*, AGU, 2010), **vol. 188,** pp. 241–264.
19. F. Klein, N. G. Grozeva, J. S. Seewald, Abiotic methane synthesis and serpentinization in olivine-hosted fluid inclusions. *Proc. Natl. Acad. Sci. U.S.A.* **116**, 201907871 (2019).
20. F. Klein, S. E. Humphris, W. Bach, Brucite formation and dissolution in oceanic serpentinite. *Geochem. Perspect. Lett.* **16**, 1–5 (2020).
21. M. Andreani *et al.*, The rocky road to organics needs drying. *Nat. Commun.* **14**, 347 (2023).
22. F. Klein *et al.*, Iron partitioning and hydrogen generation during serpentinization of abyssal peridotites from 15°N on the Mid-Atlantic Ridge. *Geochim. Cosmochim. Acta* **73**, 6868–6893 (2009).
23. J. Kodolanyi, T. Pettke, C. Spandler, B. S. Kamber, K. Gmeling, Geochemistry of ocean floor and fore-arc serpentinites: Constraints on the ultramafic input to subduction zones. *J. Petrol.* **53**, 235–270 (2012).
24. F. Deschamps, M. Godard, S. Guillot, K. Hattori, Geochemistry of subduction zone serpentinites: A review. *Lithos* **178**, 96–127 (2013).
25. P. B. Kelemen, J. M. Matter, In situ carbonation of peridotite for CO_2 storage. *Proc. Natl. Acad. Sci. U.S.A.* **105**, 17295–17300 (2008).
26. F. Klein, D. L. Goldsby, J. Lin, M. Andreani, Carbonation of serpentinite in creeping faults of California. *Geophys. Res. Lett.* **49**, e2022GL099185 (2022).
27. L. Ternieten, G. L. Früh-Green, S. M. Bernasconi, Carbonate mineralogy in mantle peridotites of the Atlantis Massif (IODP expedition 357). *J. Geophys. Res. Solid Earth* **126**, e2021JB021885 (2021).
28. F. Klein, T. M. McCollom, From serpentinization to carbonation: New insights from a CO_2 injection experiment. *Earth Planet. Sci. Lett.* **379**, 137–145 (2013).
29. F. Klein, C. J. Garrido, Thermodynamic constraints on mineral carbonation of serpentinized peridotite. *Lithos* **126**, 147–160 (2011).
30. N. G. Grozeva, F. Klein, J. S. Seewald, S. P. Sylva, Experimental study of carbonate formation in oceanic peridotite. *Geochim. Cosmochim. Acta* **199**, 264–286 (2017).
31. P. W. Gast, Trace element fractionation and the origin of tholeiitic and alkaline magma types. *Geochim. Cosmochim. Acta* **32**, 1057–1086 (1968).
32. C. H. Langmuir, J. F. Bender, The geochemistry of oceanic basalts in the vicinity of transform faults: Observations and implications. *Earth Planet. Sci. Lett.* **69**, 107–127 (1984).
33. P. J. Michael, D. W. Graham, The behavior and concentration of CO_2 in the suboceanic mantle: Inferences from undegassed ocean ridge and ocean island basalts. *Lithos* **236–237**, 338–351 (2015).
34. M. Maia *et al.*, Extreme mantle uplift and exhumation along a transpressive transform fault. *Nat. Geosci.* **9**, 619–623 (2016).
35. N. G. Grozeva, F. Klein, J. S. Seewald, S. P. Sylva, Chemical and isotopic analyses of hydrocarbon-bearing fluid inclusions in olivine-rich rocks. *Philos. Trans. A Math. Phys. Eng. Sci.* **378**, 20180431 (2020).
36. W. G. Melson, S. R. Hart, G. Thompson, "St. Paul's Rocks, Equatorial Atlantic: Petrogenesis, radiometric ages, and implications on sea-floor spreading" in *Studies in Earth and Space Sciences*, R. Shagam *et al.*, Eds. (Geological Society of America, 1972).

37. Y. Niu, Bulk-rock major and trace element compositions of abyssal peridotites: Implications for mantle melting, melt extraction and post-melting processes beneath mid-ocean ridges. *J. Petrol.* **45**, 2423–2458 (2004).
38. H. Paulick *et al.*, Geochemistry of abyssal peridotites (Mid-Atlantic Ridge, 15°20′N, ODP Leg 209): Implications for fluid-rock interaction in slow spreading environments. *Chem. Geol.* **234**, 179–210 (2006).
39. P. García del Real *et al.*, Clumped-isotope thermometry of magnesium carbonates in ultramafic rocks. *Geochim. Cosmochim. Acta* **193**, 222–250 (2016).
40. W. E. Seyfried, N. J. Pester, B. M. Tutolo, K. Ding, The Lost City hydrothermal system: Constraints imposed by vent fluid chemistry and reaction path models on subseafloor heat and mass transfer processes. *Geochim. Cosmochim. Acta* **163**, 59–79 (2015).
41. F. Klein, V. Le Roux, Quantifying the volume increase and chemical exchange during serpentinization. *Geology* **48**, 552–556 (2020).
42. B. R. Frost, J. S. Beard, On silica activity and serpentinization. *J. Petrol.* **48**, 1351–1368 (2007).
43. B. Malvoisin, Mass transfer in the oceanic lithosphere: Serpentinization is not isochemical. *Earth Planet. Sci. Lett.* **430**, 75–85 (2015).
44. N. K. Lünsdorf, J. O. Lünsdorf, Evaluating Raman spectra of carbonaceous matter by automated, iterative curve-fitting. *Int. J. Coal Geol.* **160–161**, 51–62 (2016).
45. D. G. Henry, I. Jarvis, G. Gillmore, M. Stephenson, Raman spectroscopy as a tool to determine the thermal maturity of organic matter: Application to sedimentary, metamorphic and structural geology. *Earth Sci. Rev.* **198**, 102936 (2019).
46. M. D. Lilley, D. A. Butterfield, J. E. Lupton, E. J. Olson, Magmatic events can produce rapid changes in hydrothermal vent chemistry. *Nature* **422**, 878–881 (2003).
47. J. M. McDermott, S. P. Sylva, S. Ono, C. R. German, J. S. Seewald, Geochemistry of fluids from Earth's deepest ridge-crest hot-springs: Piccard hydrothermal field, Mid-Cayman Rise. *Geochim. Cosmochim. Acta* **228**, 95–118 (2018).
48. M. Javoy, F. Pineau, The volatiles record of a popping rock from the Mid-Atlantic Ridge at 14°N:–Chemical and isotopic composition of gas trapped in the vesicles. *Earth Planet. Sci. Lett.* **107**, 598–611 (1991).
49. W. C. Shanks III, "Stable isotopes in seafloor hydrothermal systems" in *Stable Isotope Geochemistry*, J. W. Valley, D. Cole, Eds. (Mineralogical Sociey of America, 2001), pp. 469–525.
50. K. A. Aquino *et al.*, Multi-stage evolution of the Lost City hydrothermal vent fluids. *Geochim. Cosmochim. Acta* **332**, 239–262 (2022).
51. W. G. Melson, E. J. Jarosewich, R. Cifelli, Alkali olivine basalt dredged near St. Paul's rocks, Mid-Atlantic Ridge. *Nature* **215**, 381–382 (1967).
52. F. A. Frey, Rare earth and potassium abundances in St. Paul's Rocks. *Earth Planet. Sci. Lett.* **7**, 351–360 (1970).
53. J. M. Sinton, Ultramafic inclusions and high-pressure xenocrysts in submarine basanitoid, equatorial Mid-Atlantic Ridge. *Contrib. Mineral. Petrol.* **70**, 49–57 (1979).
54. R. Cifelli, "Age relationships of Mid-Atlantic Ridge sediments" in *Radiometric Dating and Paleontologic Zonation*, O. L. Bandy, Ed. (Geological Society of America, 1970).
55. T. Plank, C. Langmuir, Effects of melting regime on the composition of oceanic crust. *J. Geophys. Res.* **97**, 19749–19770 (1992).
56. T. Keller, R. F. Katz, M. M. Hirschmann, Volatiles beneath mid-ocean ridges: Deep melting, channelised transport, focusing, and metasomatism. *Earth Planet. Sci. Lett.* **464**, 55–68 (2017).
57. D. Brunelli, M. Seyler, Asthenospheric percolation of alkaline melts beneath the St. Paul region (Central Atlantic Ocean). *Earth Planet. Sci. Lett.* **289**, 393–405 (2010).
58. C. A. Rychert *et al.*, A dynamic lithosphere–asthenosphere boundary near the equatorial Mid-Atlantic Ridge. *Earth Planet. Sci. Lett.* **566**, 116949 (2021).
59. M. Anderson *et al.*, Extreme heterogeneity in mid-ocean ridge mantle revealed in Lavas From the 8°20′N near-axis seamount chain. *Geochem. Geophys. Geosyst.* **22**, e2020GC009322 (2021).
60. F. Pineau, S. Shilobreeva, R. Hekinian, D. Bideau, M. Javoy, Deep-sea explosive activity on the Mid-Atlantic Ridge near 34°50′N: A stable isotope (C, H, O) study. *Chem. Geol.* **211**, 159–175 (2004).
61. C. Aubaud, Carbon stable isotope constraints on CO_2 degassing models of ridge, hotspot and arc magmas. *Chem. Geol.* **605**, 120962 (2022).
62. T. Shibata, G. Thompson, F. A. Frey, Tholeiitic and alkali basalts from the Mid-Atlantic Ridge at 43°N. *Contrib. Mineral. Petrol.* **70**, 127–141 (1979).
63. G. D. Harper, Tectonics of slow spreading mid-ocean ridges and consequences of a variable depth to the brittle/ductile transition. *Tectonics* **4**, 395–409 (1985).
64. M. K. Roden, S. R. Hart, F. A. Frey, W. G. Melson, Sr, Nd and Pb isotopic and REE geochemistry of St. Paul's Rocks: The metamorphic and metasomatic development of an alkali basalt mantle source. *Contrib. Mineral. Petrol.* **85**, 376–390 (1984).
65. R. Hekinian *et al.*, Submersible observations of equatorial Atlantic mantle: The St. Paul Fracture Zone region. *Marine Geophys. Res.* **21**, 529–560 (2000).
66. L. M. Barão, B. Trzaskos, R. J. Angulo, M. C. de Souza, Deformation and structural evolution of mantle peridotites during exhumation on transform faults: A forced transition from ductile to brittle regime. *J. Struct. Geol.* **133**, 103981 (2020).
67. G. L. Millhollen, P. J. Wyllie, Melting relations of brown-hornblende mylonite from St. Paul's Rocks under water-saturated and water-undersaturated conditions to 30 Kilobars. *J. Geol.* **82**, 589–606 (1974).
68. S. E. Sichel *et al.*, Geophysical and geochemical evidence for cold upper mantle beneath the equatorial Atlantic ocean. *Rev. Bras. Geofís.* **26**, 69–86 (2008).
69. F. Mehouachi, S. C. Singh, Water-rich sublithospheric melt channel in the equatorial Atlantic Ocean. *Nat. Geosci.* **11**, 65–69 (2018).
70. D. Caress, D. Chayes, C. dos Santos Ferreira, MB-System: Mapping the seafloor (Monterey Bay Aquariun Research Institute, Moss Landing, CA, 2017).
71. Ö. K. Coskun *et al.*, Quantifying the effects of hydrogen on carbon assimilation in a seafloor microbial community associated with ultramafic rocks. *ISME J.* **16**, 257–271 (2022).
72. R. T. Downs, "The RRUFF project: An integrated study of the chemistry, crystallography, Raman and infrared spectroscopy of minerals" in *Proceedings of the 19th General Meeting of the International Mineralogical Association, Kobe* (International Mineralogical Association, Kobe, Japan, 2006).
73. J. R. Petriglieri *et al.*, Micro-Raman mapping of the polymorphs of serpentine. *J. Raman Spectrosc.* **46**, 953–958 (2015).
74. F. E. Lichte, A. L. Meier, J. G. Crock, Determination of the rare-earth elements in geological materials by inductively coupled plasma mass spectrometry. *Anal. Chem.* **59**, 1150–1157 (1987).
75. K. E. Jarvis, Inductively coupled plasma mass spectrometry: A new technique for the rapid or ultra-trace level determination of the rare-earth elements in geological materials. *Chem. Geol.* **68**, 31–39 (1988).
76. H. P. Longerich, G. A. Jenner, B. J. Fryer, S. E. Jackson, Inductively coupled plasma-mass spectrometric analysis of geological samples: A critical evaluation based on case studies. *Chem. Geol.* **83**, 105–118 (1990).
77. D. M. Johnson, P. R. Hooper, R. M. Conrey, "XRF analysis of rocks and minerals for major and trace elements on a single low dilution Li-tetraborate fused bead" in *Advances in X-Ray Analysis, v, 41, Le Bas, M.J,* M. J. Le Bas, Ed. (Springer New York, NY, 1999) pp. 843–867.
78. Q. Adlan, C. M. John, Clumped isotope record of individual limestone fabrics: A potential method to constrain the timing of oil migration. *Chem. Geol.* **616**, 121245 (2023).
79. Q. Adlan, A. J. Davies, C. M. John, Effects of oxygen plasma ashing treatment on carbonate clumped isotopes. *Rapid Commun. Mass Spectrom.* **34**, e8802 (2020).
80. J. M. Eiler, E. Schauble, $^{18}O^{13}C^{16}O$ in Earth's atmosphere. *Geochim. Cosmochim. Acta* **68**, 4767–4777 (2004).
81. K. W. Huntington *et al.*, Methods and limitations of "clumped" CO_2 isotope (Delta47) analysis by gas-source isotope ratio mass spectrometry. *J. Mass Spectrom.* **44**, 1318–1329 (2009).
82. W. Guo, J. M. Eiler, Temperatures of aqueous alteration and evidence for methane generation on the parent bodies of the CM chondrites. *Geochim. Cosmochim. Acta* **71**, 5565–5575 (2007).
83. A. J. Davies, C. M. John, Reducing contamination parameters for clumped isotope analysis: The effect of lowering Porapak™ Q trap temperature to below -50°C. *Rapid Commun. Mass Spectrom.* **31**, 1313–1323 (2017).
84. C. M. John, D. Bowen, Community software for challenging isotope analysis: First applications of 'Easotope' to clumped isotopes. *Rapid Commun. Mass Spectrom.* **30**, 2285–2300 (2016).
85. S. M. Bernasconi *et al.*, Background effects on Faraday collectors in gas-source mass spectrometry and implications for clumped isotope measurements. *Rapid Commun. Mass Spectrom.* **27**, 603–612 (2013).
86. S. M. Bernasconi *et al.*, InterCarb: A community effort to improve interlaboratory standardization of the carbonate clumped isotope thermometer using carbonate standards. *Geochem. Geophys. Geosyst.* **22**, e2020GC009588 (2021).
87. I. A. Müller *et al.*, Clumped isotope fractionation during phosphoric acid digestion of carbonates at 70°C. *Chem. Geol.* **449**, 1–14 (2017).
88. A. J. Davies, C. M. John, The clumped ($^{13}C^{18}O$) isotope composition of echinoid calcite: Further evidence for "vital effects" in the clumped isotope proxy. *Geochim. Cosmochim. Acta* **245**, 172–189 (2019).
89. N. T. Anderson *et al.*, A unified clumped isotope thermometer calibration (0.5–1,100°C) using carbonate-based standardization. *Geophys. Res. Lett.* **48**, e2020GL092069 (2021).
90. T. J. Wolery, "EQ3/6, A software package for geochemical modeling of aqueous systems: Package overview and installation guide (version 7.0)" (UCRL-MA-110662-Pt.1ON: DE93003359; TRN: 93:006363, Lawrence Livermore National Laboratory, 1992).
91. F. Klein, W. Bach, T. M. McCollom, Compositional controls on hydrogen generation during serpentinization of ultramafic rocks. *Lithos* **178**, 55–69 (2013).
92. F. Klein, Dataset S1 for manuscript "Mineral Carbonation of Peridotite Fueled by Magmatic Degassing in an Oceanic Transform Fault" by Frieder Klein et al. (PNAS). Zenodo. https://zenodo.org/doi/10.5281/zenodo.8329341. Version 1. Deposited 18 December 2023.